TU Delft

Delft University of Technology

Document Version
Final published version

Licence
Dutch Copyright Act (Article 25fa)

Citation (APA)
Xu, T., Ahmad, J., Liang, Y., Mouli, G. R. C., & Niasar, M. G. (2026). Design of Electrical Power Architectures for All-Electric Aircraft with Emphasis on Cabling and Battery Systems. *IEEE Transactions on Transportation Electrification* , *12*(4), 6288-6301. https://doi.org/10.1109/TTE.2026.3683126

Important note
To cite this publication, please use the final published version (if applicable).
Please check the document version above.

Copyright
In case the licence states “Dutch Copyright Act (Article 25fa)”, this publication was made available Green Open Access via the TU Delft Institutional Repository pursuant to Dutch Copyright Act (Article 25fa, the Taverne amendment). This provision does not affect copyright ownership.
Unless copyright is transferred by contract or statute, it remains with the copyright holder.

Sharing and reuse
Other than for strictly personal use, it is not permitted to download, forward or distribute the text or part of it, without the consent of the author(s) and/or copyright holder(s), unless the work is under an open content license such as Creative Commons.

Takedown policy
Please contact us and provide details if you believe this document breaches copyrights.
We will remove access to the work immediately and investigate your claim.

This work is downloaded from Delft University of Technology.

Design of Electrical Power Architectures for All-Electric Aircraft With Emphasis on Cabling and Battery Systems

Tiantian Xu, *Member, IEEE*, Jawad Ahmad, *Member, IEEE*, Yawen Liang, *Member, IEEE*, Gautham Ram Chandra Mouli, *Senior Member, IEEE*, and Mohamad Ghaffarian Niasar, *Member, IEEE*

***Abstract*—Electric aircraft represent a promising low-emission alternative to conventional fuel-powered aviation, driving the demand for lightweight and reliable electrical powertrain architectures. This study presents a design process for an electrical power system with an emphasis on the cabling system and battery in all-electric aircraft (AEA). Design considerations for the cabling system in power distribution architectures are discussed, including cable insulation material selection, conductor choice, sizing, and weight reduction methods. The influence of different system voltages and operating temperatures on cable weight is analyzed to identify optimal design tradeoffs. A comparison of polytetrafluoroethylene (PTFE) and perfluoroalkoxy (PFA) insulation materials, as well as aluminum and copper conductors, highlights their impact on weight and reliability, with PFA offering weight advantages under typical aerospace operating conditions. The batteries are sized based on the energy and power demands of a 90-seater AEA as a case study. After designing the components of the aircraft's electrical power system, the electrical architectures are presented. Furthermore, a framework for evaluating the electrical power system architectures of AEAs is proposed, using two key criteria: reliability and weight. The weight of the electrical power system is then estimated based on aircraft performance requirements. The proposed framework provides practical guidelines for cable selection and architecture optimization in future AEAs.**

***Index Terms*—All-electric aircraft (AEA), battery design, cabling system, electric power system, reliability evaluation.**

I. Introduction

THE need to reduce carbon emissions and fuel consumption [1] has driven aircraft manufacturers to seek new solutions. As a result, the development of next-generation electric aircraft, including more-electric aircraft (MEA) and all-electric aircraft (AEA), has accelerated rapidly. The MEA has already been commercialized in aircraft such as the Airbus A380 and Boeing 787, while the AEA is still a long-term goal. These aircraft require significantly higher electrical power compared with conventional designs. A high-voltage transmission architecture provides significant advantages in terms of both mass and efficiency. Recent system-level studies have shown that propulsion electrification strongly impacts material demand, component sizing, and lifecycle cost across all- and hybrid-electric aircraft concepts [2]. These higher voltage and power demands introduce new design criteria for AEA power systems. In 2024, researchers from Elysian Aircraft and Delft University of Technology proposed full battery technologies, new cabling systems, and updated electrical architecture designs [3], [4].

With the rapid advancement of aircraft electrification, onboard cabling systems are increasingly subjected to elevated electric fields and high thermal loads, imposing stringent requirements on insulation dielectric strength and temperature capability. While increasing insulation thickness can reduce the risk of dielectric failure, it also introduces a significant weight penalty, making insulation design a critical trade-off between electrical reliability and lightweight objectives. Consequently, insulation and conductor selection must be evaluated in conjunction with system voltage level, operating temperature, and power demand, rather than by empirical margins alone. Although fluoropolymers such as PTFE and PFA are widely regarded as promising candidates for next-generation aircraft cabling due to their favorable dielectric and thermal properties [5], recent work on MVDC cable design for AEA has concentrated on conductor size optimization or multilayer insulation geometry [3], [6], [7], without providing a systematic electrothermal comparison of these materials across different voltage levels and operating temperatures that directly inform cable sizing and weight tradeoffs. This study addresses this gap by establishing an integrated electrothermal framework for the quantitative comparison of conductor and insulation materials in AEA power distribution systems. Moreover, as the primary energy source within the AEA powertrain, the battery pack must be sized to meet mission power and energy requirements while satisfying constraints such as the empty weight ratio, and it is the most critical component determining overall powertrain weight [8], [9].

While power from the engine is transformed into hydraulic, mechanical, and pneumatic power sources in traditional

Received 17 December 2025; revised 2 February 2026 and 12 March 2026; accepted 4 April 2026. Date of publication 14 April 2026; date of current version 22 July 2026. This work was supported in part by Dutch Nationaal Groeifonds (NGF) under Grant 31194660. *(Corresponding author: Mohamad Ghaffarian Niasar.)*

Tiantian Xu, Jawad Ahmad, and Mohamad Ghaffarian Niasar are with the High Voltage Technologies, Department of Electrical Sustainable Energy, Delft University of Technology, 2628 CD Delft, The Netherlands (e-mail: T.Xu-1@tudelft.nl; J.Ahmad@tudelft.nl; M.GhaffarianNiasar@tudelft.nl).

Yawen Liang and Gautham Ram Chandra Mouli are with the DC Systems, Energy Conversion and Storage Group, Department of Electrical Sustainable Energy, Delft University of Technology, 2628 CD Delft, The Netherlands (e-mail: Y.Liang-3@tudelft.nl; G.R.ChandraMouli@tudelft.nl).

Digital Object Identifier 10.1109/TTE.2026.3683126

2332-7782 © 2026 IEEE. All rights reserved, including rights for text and data mining, and training of artificial intelligence and similar technologies. Personal use is permitted, but republication/redistribution requires IEEE permission.
See https://www.ieee.org/publications/rights/index.html for more information.

Authorized licensed use limited to: TU Delft Library. Downloaded on August 13,2026 at 11:22:15 UTC from IEEE Xplore. Restrictions apply.

aircraft [10], AEAs must convert all of these systems into electrical systems. In AEAs, this demand requires higher voltage levels to efficiently deliver the required power [5]. To address these challenges, various electrical architectures and power management strategies have been proposed for the design of AEAs and MEAs, including cross-redundant structures, ring structures, direct structures, and H-type structures, as well as distributed and fault-tolerant power management frameworks [3], [11], [12], [13], [14], [15], [16]. These architectures differ in reliability and weight performance [13], [14], [15]. However, existing studies on aircraft electrical power system architectures mainly evaluate architectures using a single performance criterion, either reliability or weight [13], [14], [15]. Reliability analysis is a critical requirement for the electrical architecture design in AEAs [14], [17], [18], while weight evaluation is essential for achieving efficient and feasible aircraft designs [13]. Consequently, current studies provide limited guidance for architecture selection when both lightweight design and reliability requirements must be satisfied. To address this gap, this study introduces an integrated evaluation framework that considers reliability and weight for the comparison of electrical power distribution architectures in AEAs. The proposed framework enables a more realistic and system-level assessment of electrical power system designs for AEA.

This article is organized as follows. Section II presents the design process of electrical components, with an emphasis on the cabling system and battery. The cable insulation material selection, conductor choice, sizing, and weight reduction methods are discussed in detail. This article compares PTFE and PFA insulation materials in terms of their impact on weight and reliability. It analyzes the effect of different system voltages and operating temperatures on cable weight and discusses battery design based on power requirements. Section III briefly addresses other components, such as power converters, and details the electrical architecture for AEAs. The power distribution architecture is designed based on a 90-seater AEA. Moreover, a detailed evaluation process is presented to assess reliability and weight. In Section IV, the key conclusions of this study are summarized.

II. Component Design in AEA Power Systems

The electrical power system is designed to transmit power from the generators and batteries to the electric motors, as well as other onboard electrical loads. In general, the core components of an AEA power distribution system include the battery, electric motors, generators, DC–DC converters, DC–AC inverters, AC–DC converters (rectifiers), safety switches, and the cabling network. As a case study, the Elysian E9X aircraft is introduced as a conceptual design for a 90-seater fully electric aircraft, featuring turbo generators, battery modules, and eight electric propellers [19].

A. Cable Design

The primary design constraint for AEAs at the current technological stage is weight. Currently, electric motors are limited in their ability to generate sufficient thrust for aviation applications due to their low power-to-weight ratio, primarily resulting from the high mass and low energy density of existing battery technologies. Given current battery technology limitations, some improvement in energy density is feasible; for instance, advancements could allow an increase from 250 to around 500 Wh/kg. However, reaching levels like 10 000 Wh/kg remains far beyond current capabilities. Therefore, while modest reductions in battery mass are possible, significant weight optimization must still primarily focus on other aircraft components. In the propulsion drivetrain, this optimization is particularly crucial for the cabling system. Minimizing cable weight by reducing the quantity of cables can compromise redundancy, making it essential to ensure that individual cables are as lightweight as possible. This section examines the design parameters of the transmission network cabling, including conductor material selection, heat dissipation during operation, conductor sizing based on voltage and power requirements, and insulation specifications. Ultimately, the mass per meter of cable kg/m is determined for different power levels, which is used to calculate the overall weight of the cabling system for topology comparison, as described in Section III.

TABLE I
Thermal–Electrical Variables and Constants Used in the Cable Model

Symbol	Description	Unit / Value
Dependent (solved) variables		
r_c	Conductor radius	mm
t_i	Insulation thickness	mm
Independent (swept) variables		
T_c	Conductor temperature (abs.)	K
T_s	Surface temperature (abs.)	K
h	Convection heat transfer coeff.	W $m^{-2}K^{-1}$
V	System voltage	0.8–3 kV
P	Power on cable	MW
Controlled (fixed) parameters		
T_{amb}	Ambient temperature	313 K (40°C)
ν	Air kinematic viscosity	2.65×10^{-5} m^2/s [20]
λ	Air convection coefficient	2.7×10^{-2} W/mK
σ_{SB}	Stefan–Boltzmann constant	5.67×10^{-8} W $m^{-2}K^{-4}$ [21]
ε	Insulation emissivity	0.8 [3]
Pr	Prandtl number (air)	0.71 [22]
t_{isc}, t_{osc}	Semiconducting layers	0.25 mm
t_s, t_{oj}	Sheath and outer jacket	1 mm

The thermal–electrical cable sizing involves a set of unknown design variables to be solved, a set of independent variables that are swept to study their influence, and a set of controlled parameters that are fixed according to environmental conditions and material properties. For clarity and reproducibility, all variables, symbols, units, and reference sources are summarized in Table I.

1) Cable Conductor Design:

a) Cable conductor material considerations: Copper and aluminum are the primary conductors used in cable design, each offering distinct advantages. Copper has a conductivity of approximately 58 MS/m, compared to aluminum 36 MS/m, giving it around 60% higher electrical conductivity. However, copper is significantly heavier, with a density of 8.96 g/cm^3 compared to aluminum 2.70 g/cm^3. This significant weight difference makes aluminum preferable in aerospace applica-

Authorized licensed use limited to: TU Delft Library. Downloaded on August 13,2026 at 11:22:15 UTC from IEEE Xplore. Restrictions apply.

tions, where mass reduction is critical to performance and efficiency. The choice balances electrical performance against mass efficiency.

b) Cable conductor sizing: The sizing of the cable conductor is primarily determined by the maximum current it must carry. In addition, the temperature rise resulting from the conductor's electrical resistance must be taken into account during the conductor sizing process. The resistance per unit length of the cable conductor can be expressed as

$$R/l = 1/\sigma_c S \tag{1}$$

where R is the conductor resistance (Ω), l is the cable length (m), σ_c is the conductor conductivity ($S \cdot m^{-1}$), and S is the cross-sectional area of the conductor (m^2). The actual resistance of the conductor (R_c) is affected by the operating temperature, and their relationship is described as [20], [23]

$$R_c = R_{ref} \cdot (1 + \alpha_r (T_c - T_{ref})) \tag{2}$$

where T_c is the actual conductor temperature, defined as the maximum allowable temperature under operating conditions. α_r is the resistance–temperature coefficient ($°C^{-1}$). R_{ref} is the reference resistance at a given temperature T_{ref}, and the equation for R_{ref} is

$$R_{ref} = \rho \cdot l/S = \rho \cdot l/\left(\pi r_c^2\right) \tag{3}$$

where ρ is the resistivity ($\Omega \cdot m$) of the conductor at the reference temperature and r_c is the conductor radius (m). To determine the optimal conductor radius, a key parameter influencing cable performance, thermal losses, and system parameters must be carefully analyzed.

c) Heat dissipation and thermal considerations: Due to the high power levels transmitted through the conductor, the resulting current flow generates significant heat, raising the conductor's temperature. The insulator must effectively dissipate this heat through the insulation and other layers of the cable to the environment in order to ensure continuous and stable cable operation, preventing potential failures or fire hazards. The total heat loss from the conductor, primarily through convection and radiation, must be balanced with the heat generated by the current flowing through the cable. These relationships are represented by the following equations [21]

$$Q_c = Q_{convection} + Q_{radiation} = \frac{I^2}{\sigma_c \cdot \pi \cdot r_c^2} \tag{4}$$

$$Q_{convection} = h \cdot A \cdot (T_s - T_{Amb}) \tag{5}$$

$$Q_{radiation} = \epsilon \cdot \sigma_{SB} \cdot A \cdot \left(T_s^4 - T_{Amb}^4\right) \tag{6}$$

where Q_c is the total heat produced by the conductor, I is the current in the cable, $Q_{convection}$ is the heat loss due to convection, Q_{rad} is the heat loss due to radiation, and A is the outer area exposed (m^2). The parameters including T_s, T_{amb}, ε, and σ_{SB} are described in Table I.

The use of natural convection with radiation and T_{amb} = 40 °C was chosen intentionally as a conservative boundary condition for cable sizing to avoid underestimating conductor temperature and cable cross-section. This corresponds to a hot-day, ground/near-ground worst case or highest ambient temperature the aircraft may encounter at departure locations. In practice, T_{amb} varies with altitude, location, and local installation environment (ducting, proximity to heat sources). In practical aircraft installations, some cable routing locations may experience forced convection due to ventilation airflow or aircraft motion. Under such conditions, the convective heat transfer coefficient h may increase from typical natural convection values of approximately 5–10 to 20–50 $W\,m^{-2}K^{-1}$ in ventilated compartments or ducts. A higher heat transfer coefficient enhances heat dissipation from the cable surface, reducing the temperature rise for a given current, thereby allowing a higher permissible current density. This enables a reduction in conductor cross-section for a given power level, which can directly lead to lower cable weight and improved power-to-weight efficiency. However, since airflow conditions strongly depend on installation geometry and aircraft configuration, this work adopts natural convection as a conservative baseline. Forced convection conditions may further enhance heat dissipation and reduce cable weight; however, their quantitative impact is highly dependent on installation-specific airflow conditions, routing geometry, and cooling configurations. Quantifying the exact weight reduction achievable under forced convection would require detailed airflow modeling and installation-specific data and is not explicitly evaluated in this study and, therefore, beyond the scope of this study. Nevertheless, the proposed framework can be readily extended to forced convection conditions by substituting an appropriate heat transfer coefficient h derived from airflow correlations or experimental measurements. In our case, h is the convection thermal coefficient, which is derived using the Nusselt relation [21], [24]

$$Nu = \frac{hl}{\lambda} = 0.12\,(Gr \cdot Pr)^{1/3} \tag{7}$$

where Gr is the Grashof number defined as follows:

$$Gr = \frac{gl^3\beta\Delta T}{\nu^2} \tag{8}$$

where g is the gravitational constant and β is the gas expansion coefficient, approximated as the inverse of the average temperature for an ideal gas [25]. By combining and rearranging these equations, the final expression for the convective heat transfer coefficient is obtained

$$h = 0.12\lambda \cdot \left(\frac{g}{\nu^2} \cdot \beta \cdot (T_s - T_{Amb}) \cdot Pr\right)^{\frac{1}{3}}. \tag{9}$$

At steady state, the temperature difference between the conductor and the surface, and the surface and the surroundings (ambient temperature) is represented by the following relationships [24], [26]:

$$T_c - T_s = \frac{I^2}{\sigma_c \pi r_c^2} \cdot \left[\frac{1}{2\pi k_{tef}} \ln\left(\frac{r_c + t_{isc} + t_i + t_{osc}}{r_c}\right) + \frac{1}{2\pi k_{tef}} \ln\left(\frac{r_c + t_{isc} + t_i + t_{osc} + t_s + t_{oj}}{r_c + t_{isc} + t_i + t_{osc} + t_s}\right)\right] \tag{10}$$

$$T_s - T_{amb} = \frac{I^2}{\sigma_c\, 2\pi^2\, r_c^2\, h\, \left(r_c + t_{isc} + t_i + t_{osc} + t_s + t_{oj}\right.} \tag{11}$$

Authorized licensed use limited to: TU Delft Library. Downloaded on August 13,2026 at 11:22:15 UTC from IEEE Xplore. Restrictions apply.

TABLE II
PROPERTIES OF PTFE AND PFA INSULATION MATERIALS

Material Properties	PTFE	PFA
Electrical Properties		
Permittivity	2.1	2.1
Dielectric strength (kV/mm)	60∼80	70∼80
Material density (kg/m^3)	2170	2150
Thermal Properties		
Thermal conductivity (W·m^{-1}·K^{-1})	0.25	0.19
Melting point (°C)	327	305
Temperature range (°C)	-90∼+260	-90∼+260
Mechanical Properties		
Modulus of elasticity (GPa)	0.49	0.55
Tensile strength (MPa)	24	28
Flexibility	Moderate	High
Flex life	Excellent	Good

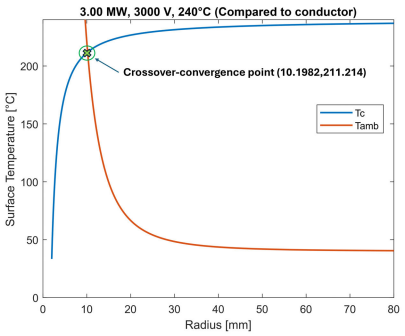


Fig. 1. Surface temperature T_s as a function of conductor radius r_c.

where k_{tef} is the thermal conductivity of the polymer insulating layer (listed in Table II). The parameters including t_{isc}, t_{osc}, t_i, t_s, and t_{oj} are described in Table I.

MATLAB was used to solve these nonlinear sets of simultaneous equations in a graphical manner through substitution. By performing a series of calculations, the relationship between conductor radius and conductor temperature under specified voltage and current conditions was determined. In order to obtain a correct value for the surface temperature, both (10) and (11) are plotted for a series of conductor radii and solved simultaneously. The resulting crossover point is then the solution of the equations, the required conductor radius, and surface temperature combination. The resultant conductor radius is finally used to evaluate the weight of the cable. As an example, the steady-state (surface) temperature for a 3-kV system and a conductor temperature of 240 °C as a function of the conductor radius is shown in Fig. 1.

To enable a comparative analysis across different conditions, a range of independent variables was selected. Specifically, a range of conductor temperature cases was considered (e.g., 90 °C–240 °C). In addition, the temperature for conductor sizing was considered to be 150 °C, ensuring reliable operating performance while maintaining thermal stability. Furthermore, the maximum allowable temperature for conductor sizing was limited to 200 °C, which can be observed under extreme conditions (heavy load). These temperatures were chosen to provide a balanced reference for determining the optimal conductor radius while accounting for potential temperature variations. In addition, a range of system voltage levels (e.g., 800 V–3 kV) was selected for evaluation. This selection ensures a comprehensive assessment of conductor sizing under different operating conditions.

2) Cable Insulation Design: The insulation layer is a crucial component of the cable, serving both thermal and electrical functions. Insulation mitigates the thermal effects of the conductor current while also withstanding the high electric field induced by the high voltages applied to the cable. For AEA cables, several challenges arise due to higher voltages and currents, including arcing and arc tracking, partial discharge (PD), and thermal management. Unlike ground-based MVDC grids and submarine cables, aviation cables operate across a wider temperature range. The minimum high-temperature tolerance for aerospace applications should be at least 150 °C [3], [27]. In addition, during high-altitude flights, the breakdown voltage of air decreases as pressure drops, increasing the risk of arcing and PD, making insulation selection even more critical.

a) Comparison of insulation materials: Table II compares the properties of various insulation materials suitable for electric aircraft applications [28], [29], [30]. Several high-performance polymers have been considered for AEA cable insulation, including polytetrafluoroethylene (PTFE), perfluoroalkoxy (PFA) polymer, cross-linked ethylene tetrafluoroethylene (XL-ETFE), and polyimide (PI). These materials provide strong resistance to arc tracking and high thermal stability. Among them, PTFE and PFA are widely used in aerospace wiring. As summarized in Table II, PTFE and PFA exhibit similar electrical and thermal properties. PFA offers slightly higher tensile strength and improved flexibility, facilitating cable routing in aircraft wiring harnesses. While PTFE generally provides higher flex fatigue resistance under extreme cyclic bending, PFA still provides sufficient flex life for typical aircraft cable configurations. In addition, PFA has a slightly lower density and is melt-processable, enabling thin-wall insulation and supporting lightweight cable designs. Therefore, PTFE and PFA remain strong candidates for AEA high-voltage cabling systems, offering a balance between thermal stability, arc tracking resistance, mechanical performance, and weight reduction.

b) Insulator sizing: The single void discharge (SVD) method is used to calculate insulation thickness, allowing a unified analysis for both copper and aluminum conductors as it is independent of conductor material [31]. SVD explicitly accounts for microscopic voids and defects within polymeric insulation and ensures discharge-free operation, which is critical for long-term reliability under MVDC stress and fast inverter voltage transients. Compared to field-stress-only or breakdown-based approaches, the SVD criterion provides a more conservative and physically motivated insulation sizing, particularly relevant for low-pressure aircraft environments where PD inception voltage is reduced. The insulation thickness primarily depends on the maximum applied voltage, given

Authorized licensed use limited to: TU Delft Library. Downloaded on August 13,2026 at 11:22:15 UTC from IEEE Xplore. Restrictions apply.

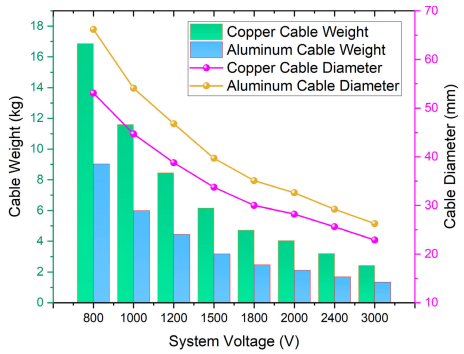


Fig. 2. Cable weight and diameter under different system voltages.

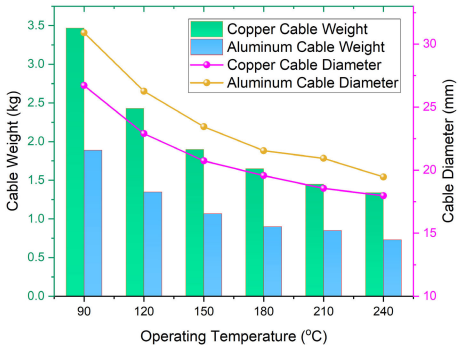


Fig. 3. Cable weight and diameter at different operating temperatures.

by the following equation:

$$t_i = r_c \cdot \left(\exp\left(\frac{K \cdot V \cdot t_v}{\alpha \cdot r_c} \right) - 1 \right) + C. \tag{12}$$

The thickness of the void or inclusion (t_v) is assumed to be 50 μm [31], and V is the system voltage level, while α represents the minimum breakdown voltage of air in the cavity, taken as 250 V [32]. This represents the worst case value for the breakdown voltage corresponding to a low-pressure environment typically observed at cruise altitudes (approximately 7–10 km), where PD activity is critical. The shape factor (K) is assumed to be spherical. The equation is expressed as follows:

$$K = \frac{3\varepsilon}{1 + 2\varepsilon} \tag{13}$$

where ε is the permittivity of the insulator.

3) Cable Weight Estimation: The total cable weight is determined by contributions from its main components: the conductor, the insulator, the metal sheath, and the outer jacket. The estimation method relies on the material densities within the cable. The conductor mass is calculated using the density of the conductor material (ρ_c), the selected conductor cross-sectional area (A), and the cable length (l), as described in (14)–(17). Once the final layer dimensions are determined, their respective weights can be calculated

$$\text{Conductor mass} = \rho_c \cdot l \cdot \pi \cdot r_c^2 \tag{14}$$

$$\text{Insulator mass} = \rho_{\text{insul}} \cdot l \cdot \pi \cdot \left((r_c + t_{isc} + t_i + t_{osc})^2 - r_c^2 \right) \tag{15}$$

$$\text{Sheet mass} = \rho_{\text{alum}} \cdot l \cdot \pi \cdot \left[(r_c + t_{isc} + t_i + t_{osc} + t_s)^2 - (r_c + t_{isc} + t_i + t_{osc})^2 \right] \tag{16}$$

$$\text{Jacket mass} = \rho_{\text{insul}} \cdot l \cdot \pi \cdot \left[\left(r_c + t_{isc} + t_i + t_{osc} + t_s + t_{oj} \right)^2 - (r_c + t_{isc} + t_i + t_{osc} + t_s)^2 \right] \tag{17}$$

$$m_{\text{total}} = \text{conductor mass} + \text{insulator mass} + \text{sheet mass} + \text{jacket mass}. \tag{18}$$

a) Weight and diameter variations with voltage: Fig. 2 illustrates the impact of voltage on cable weight and diameter. Although aluminum cables require a larger conductor radius, they remain significantly lighter than their copper counterparts. At 800 V, the total weight of the copper cable is 16.87 kg, while the aluminum cable weighs only 9.03 kg. When the voltage is increased to 3 kV, the copper cable weight drops to 2.43 kg, and the aluminum cable further reduces to 1.35 kg. The weight reduction benefits of higher voltage levels are particularly pronounced for copper cables. In terms of cable diameter, the aluminum cable diameter is 13.12 mm larger than that of the copper cable, estimated at 800 V. As the voltage increases, at 3 kV, the aluminum cable diameter is 3.36 mm larger than that of the copper cable. This analysis confirms that both system voltage level and conductor material play a crucial role in cable weight optimization. The optimal combination of 3 kV and an aluminum conductor results in the lightest configuration, achieving a 44.4% weight reduction, making it the most effective choice for electric aircraft applications.

b) Effect of operating temperature: Fig. 3 illustrates the influence of maximum operating temperature on cable weight and dimensions. Increasing the operating temperature reduces both the weight and diameter of the cable. Raising the allowable operating temperature relaxes the thermal constraints on conductor sizing and insulation requirements, enabling a more compact and lightweight cable design. However, as the temperature rises, the weight and diameter reduction rate gradually diminish. While higher operating temperatures theoretically improve weight efficiency in aircraft applications, it is generally recommended to limit temperature rise to below 40 °C under normal operation. This supports choosing 150 °C as a balanced, conservative design point rather than pushing closer to material maximum. Despite the absence of specific standards for AEA cable design, a minimum operating temperature of 150 °C is considered a conservative and safe choice for aerospace applications based on the available aerospace wiring practice/standards [ASTM aircraft EWIS practice, SAE wire specifications standared (AS22759D) and IEC standard 60502-2)] cited in the research [3].

Several factors influence the cable's dynamic temperature rating, including operating environment, response time of protective devices, and thermal overload capability. The highest temperature rise typically occurs during short circuits on transmission lines. To mitigate risks, protective devices such as circuit breakers should be integrated into the system. When a full discharge occurs, the current flows through the

Authorized licensed use limited to: TU Delft Library. Downloaded on August 13,2026 at 11:22:15 UTC from IEEE Xplore. Restrictions apply.

insulation and into the shield. The heat generated by a short circuit current is dependent on the resistance, and the extra heat caused by the short current (Q_{short}) can be expressed as follows:

$$Q_{\text{short}} = I_{\text{short}}^2 R_{sc} \Delta t_{CB} = m_s C' \Delta T \tag{19}$$

where I_{short} is the short current, R_{sc} is the resistance of the short circuit, Δt_{CB} is the response time of circuit breaker, and C' is the specific heat capacity (J/kg·°C). Then, the extra temperature rise ΔT caused by a short circuit can be deduced from (19). It is noted that $T_{\text{operating}} + \Delta T$ should not exceed 260 °C, which is the maximum tolerance temperature of insulation. As discussed earlier, an operating temperature of 150 °C is selected as a safe design value to ensure sufficient thermal headroom. This allows additional temperature rise during short circuit events without surpassing the 260 °C, which is the thermal limit of high-performance insulation materials, such as PTFE and PFA. Using a 1-mm-thick metallic shielding layer, the corresponding allowable circuit breaker response time can be extended to approximately 3.05 ms, which is reasonable for the circuit breaker to provide enough time reacting, while still maintaining the integrity of the insulation. This configuration ensures safe, reliable cable operation even under fault conditions.

During takeoff and initial climb, the propulsion system may impose short-duration overloads, leading to a temporary rise of the conductor temperature above its steady-state operating limit. During this period, the conductor temperature may reach up to 240 °C for durations on the order of 10–15 min. To examine the applicability of the steady-state thermal model under such conditions, the corresponding surface temperature was evaluated at 240 °C, as shown in Fig. 1. For a cable designed with a continuous operating limit of 150 °C, the transient increase of the conductor temperature to 240 °C results in a maximum insulation temperature of approximately 240 °C and a peak cable surface temperature of 211.21 °C, as shown in Fig. 1. These values remain below the maximum allowable temperature of the selected fluoropolymer insulation, indicating that short-term thermal excursions associated with transient power demands do not lead to insulation overstress. This demonstrates that the steady-state design based on a 150 °C continuous rating provides sufficient thermal margin to accommodate transient and environmental variations while acknowledging that a fully time-dependent electrothermal model would be required for a detailed prediction of temperature evolution during such overload events.

c) Weight distribution across cable layers: The effect of system voltage (V) on insulation thickness is shown in Fig. 4. It can be seen that the thickness of the insulation increases with an increase in system voltage. At higher system voltages, the thickness of the insulation contributes more toward the weight of the insulation system and consequently toward the weight of the cable.

Fig. 5 presents the weight decomposition of different cable layers under varying current conditions. The proportion of conductor weight differs significantly between copper and aluminum cables. Copper cables have a higher conductor weight proportion compared to aluminum cables. At lower

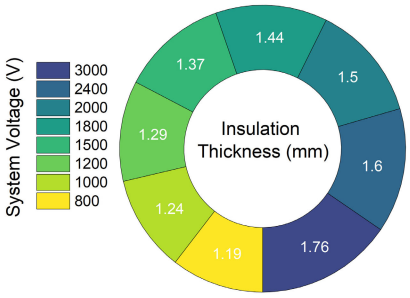


Fig. 4. Variation of insulation thickness with system voltage.

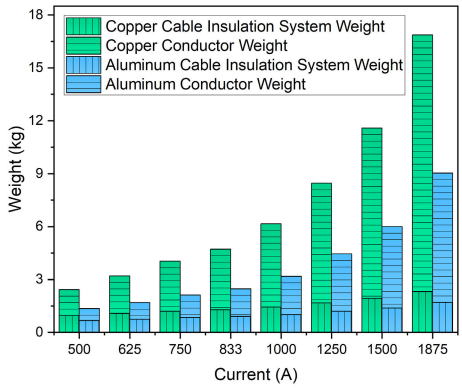


Fig. 5. Cable weight variation across various current levels.

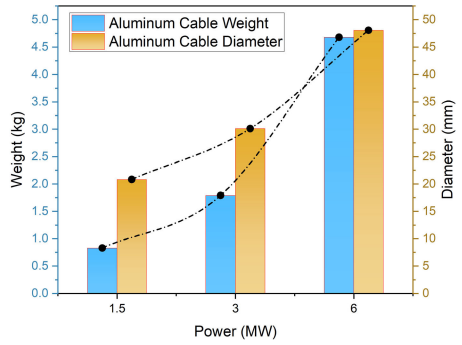


Fig. 6. Cable weight and diameter across various power levels.

current values, the mass of the insulation system contributes more toward the total weight of the cable. As the current increases, the conductor's share of total cable weight becomes more dominant. At 1875 A, the copper conductor accounts for over 80% of the total cable weight, while the aluminum conductor constitutes more than 60%.

d) Impact of power levels on cable sizing: The power levels in the system depend on the grid topology and the cable's location within the network. The continuous power rating of the motor is 1.5 MW, with a normal operating current of approximately 500 A. However, in the event of an emergency requiring backup power, which represents the worst case scenario, both generators will be engaged to supply (6 MW) power to eight motors, significantly increasing the current demand on the generator side cables. As illustrated in Fig. 6, an increase in power demand from 1.5 to 6 MW results in a significant rise in both cable weight and diameter, reflecting

Authorized licensed use limited to: TU Delft Library. Downloaded on August 13,2026 at 11:22:15 UTC from IEEE Xplore. Restrictions apply.

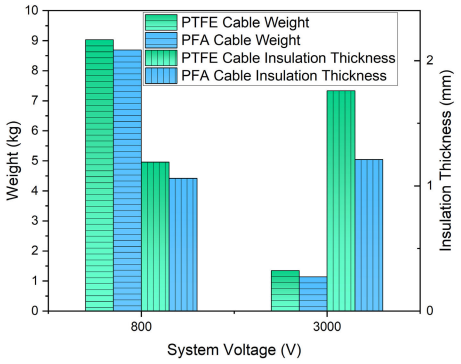


Fig. 7. PTFE and PFA cable parameters at different system voltages.

the need for larger conductor sizes to accommodate higher currents. The worst case scenario requires cables to handle significantly higher current levels (2000 A), contributing to a sharp rise in cable size and weight.

From the cable sizing perspective, two important considerations can be made. First, motor-to-bus bar and battery-to-bus bar cables can be sized for a rated current of 500 A under normal conditions. Second, cables connected to the generator side must handle high current levels, e.g., 2000 A, under emergency scenarios. Using multiple cables with smaller sizing in power sharing can contribute to the overall reduction in weight of the power cables connected to the generator side [3]. This analysis highlights the critical role of cable sizing in ensuring system reliability, particularly in the generator-side connections, where higher current-carrying capacity is necessary to account for contingencies and grid failures.

e) Cable insulation materials considerations: Fig. 7 shows a comparison of PTFE and PFA insulation materials in terms of cable weight (kg) and insulation thickness (mm) under 800-V and 3-kV system voltage levels. At 800 V, both PTFE and PFA cables have significantly higher weight and thinner insulation compared to their counterparts at 3 kV. When the voltage is increased to 3 kV, both materials show substantial reductions in cable weight. At both system voltage levels (800 V and 3 kV), PTFE cables are found to be heavier than PFA cables, indicating that PFA contributes to lower total cable weight. Insulation thickness is also greater for PTFE than PFA, reinforcing that PFA enables weight reduction through lower density and thinner insulation layers. PFA demonstrates better weight efficiency, making it a preferable choice where weight reduction is critical. However, tradeoffs in durability and flex-life need further consideration.

The proposed framework is intended for direct application in aircraft design workflows and accounts for the extreme environmental conditions encountered during operation. As discussed earlier, the thermal design assumes a conservative ambient temperature of $T_{\text{amb}} = 40\ ^{\circ}\text{C}$, representing hot ground or near-ground departure conditions, while the insulation design considers the most critical low-pressure environment at typical cruising altitude (approximately 7–10 km), where PD inception is most likely. By combining these worst case thermal and dielectric assumptions, the framework ensures that the cable design remains robust across the full operational envelope, from hot ground conditions to cold high-altitude flight. Given system-level inputs such as power demand, voltage level, allowable operating temperature, and installation conditions, the electrothermal model can be used to determine conductor cross-section, insulation thickness, and cable weight. Environmental factors such as cooling conditions (natural or forced convection), routing configuration, and altitude-dependent effects can be incorporated through appropriate boundary conditions. This enables consistent evaluation of design tradeoffs in real aircraft applications.

B. Battery Design

Considering the different phases of the flight profile, the battery pack size for the AEA can be determined using the performance specifications. A typical flight profile for an aircraft consists of five distinct phases: takeoff, climb, cruise, descent, and landing. In this study, only the first four phases are considered, as the landing phase involves minimal energy consumption and lower power demand. To simplify the analysis, the transitional periods between flight phases are neglected [9]. The sizing method is based on the validated framework in [33].

The performance requirements of the takeoff phase are often characterized by a specified takeoff run length L_{to} and takeoff speed V_{to} [33]. This can be predicted by evaluating the aircraft's acceleration along the runway, which is based on horizontal force equilibrium, as illustrated in (20). The forces involved in this process include the thrust provided by the propulsion system T, the aerodynamic drag resisting the aircraft's motion D, and friction F

$$\frac{dV}{dt} = \frac{T - D - F}{M_{\text{to}}} \tag{20}$$

where dV/dt is the linear acceleration along the runway and M_{to} is the takeoff mass of the designed AEA. During the takeoff phase, it is reasonable to assume that the motor power remains relatively constant. A practical approach is to utilize the maximum motor power P_{em} values provided by the manufacturer for takeoff calculations [9]. In practice, for scenarios involving multiple motors, the total maximum motor power P_{em} is determined by summing the maximum power of each individual motor.

Thrust T varies with velocity V and propeller efficiency η_{prop}, which change significantly during the takeoff phase. The propeller efficiency η_{prop} is further influenced by the thrust coefficient T_{c}, as detailed in [33]. Aside from the varying propeller efficiency during takeoff, this study assumes constant efficiencies for the remaining powertrain components, such as electric motors. This simplification is acceptable for high-level preliminary analysis, as electric drives combined with active control allow the propeller to operate near its optimal efficiency across different flight conditions [34].

In the climb, descent, and cruise phases, a general expression for the required power can be obtained based on the equilibrium of all the forces acting upon an aircraft [35]

$$P_{\text{i}} = \frac{W_{\text{to}} V_{\text{v,i}} + \left(\frac{1}{2}\rho^{\text{i}} S V_{\text{i}}^3 C_{\text{D0}}^{\text{i}} + K^{\text{i}} \frac{W_{\text{to}}^2}{\frac{1}{2}\rho^{\text{i}} S V_{\text{i}}}\right)}{\mu_{\text{s}}}. \tag{21}$$

Authorized licensed use limited to: TU Delft Library. Downloaded on August 13,2026 at 11:22:15 UTC from IEEE Xplore. Restrictions apply.

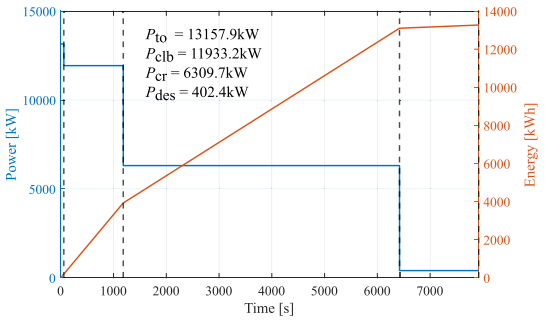


Fig. 8. Power and energy profile of the AEA battery.

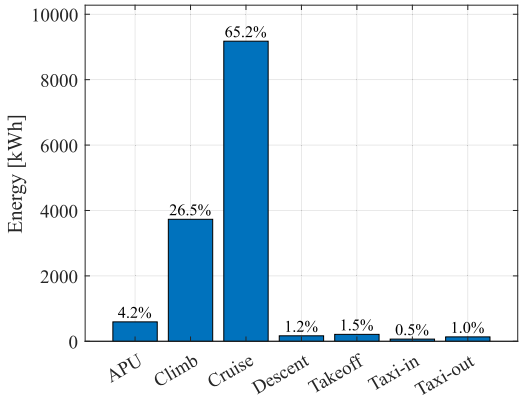


Fig. 9. Battery energy breakdown by mission segment.

$V_{v,i}$ denotes the vertical velocity, which is zero during cruise phases. ρ^i is the air density. V_i is the true airspeed. C^i_{D0} and K^i are the zero-lift drag coefficient and induced drag correction factor, respectively. μ_s is the overall system efficiency, which is the product of the propeller efficiency and combined mechanical efficiency. The subscript i denotes each flight phase.

In addition to the propulsive energy demand, the aircraft requires auxiliary electrical and mechanical power, which is supplied by the auxiliary power unit (APU). The corresponding energy consumption, denoted as E_{apu}, is assumed to be 3 kW per passenger [4], [36]. Furthermore, additional energy fractions of 1% of the taxi-out energy $E_{taxiout}$ and 0.5% of the taxi-in energy E_{taxiin} are considered [4]. Besides, a maximum depth of discharge of 90% is assumed, meaning that the battery is operated within a state-of-charge window of approximately 5%–95% [4]. Consequently, the size of the battery pack for the AEA can be determined using (22)

$$\begin{aligned}
&E_{pack,BOL} \times 0.9 \\
&= E_{to} + E_{clb} + E_{cr} + E_{des} + E_{apu} + E_{taxiout} + E_{taxiin} \\
&E_{apu} = 3\ \text{kW} \times T_{tot} \times PAX \\
&T_{tot} = T_{to} + T_{clb} + T_{cr} + T_{des} \\
&T_{cr} = \frac{R}{V_{cr}}, T_{clb} = \frac{(h_{cr} - h_a)}{V_{v,clb}}, T_{des} = \frac{(h_{cr} - h_a)}{V_{v,des}} \\
&E_{to} + E_{clb} + E_{cr} + E_{des} = E_{prop} \\
&\frac{E_{prop}}{1 - 1\% - 0.5\%} = E_{prop} + E_{taxiout} + E_{taxiin}
\end{aligned} \tag{22}$$

where PAX denotes the number of passengers ($PAX = 90$); T_{tot} is the total mission time across the takeoff, climb, cruise, and descent phases; and the total energy consumed over these phases is denoted by E_{prop}. The takeoff time T_{to} is the time duration required to accelerate the aircraft to the takeoff speed V_{to} within the specified takeoff run length L_{to}; further details can be found in [33].

Based on the equations and the data from Tables III and IV, the battery energy and power profile of the 90 pax AEA are obtained, as illustrated in Fig. 8. The calculated battery size, E_{bat}, is 15 648 kWh. The total required battery weight is 35 563.6 kg, considering the energy density of 440 Wh/kg at the pack level, which accounts for the integration of the thermal management system, battery management system, and packaging [4]. Considering the payload and takeoff weight defined in Table III, the resulting empty weight ratio is 0.47, which falls within the typical range for narrow-body aircraft [9]. The battery energy breakdown by mission segment is shown in Fig. 9. The percentage above each bar represents the energy consumed in each segment relative to the usable battery capacity, as defined by the maximum depth of discharge.

Using the baseline mission sizing, the required pack energy at beginning-of-life (BOL) is $E_{pack,BOL}$ = 15 648 kWh.

TABLE III
PERFORMANCE INDICES OF THE AEA [4], [19], [37]

Model	AEA
Wing area	150 m^2
Wing span	42 m
Propeller diameter	118.11 inch
RPM	1200
Motor power	1500 kW
Motor number	8
Takeoff weight W_{to}	76 000 kg
Payload weight W_{to}	9000 kg
Friction coefficient μ	0.03
Lift coefficient during takeoff C^{to}_L	1.7
Zero-lift drag coefficient C^{to}_{D0}, C^{clb}_{D0}, C^{des}_{D0}, C^{cr}_{D0}	0.011
Rate of climb $V_{v,clb}$	6.67 m s^{-1}
Rate of descent $V_{v,des}$	5.00 m s^{-1}
Climb/Descent speed V_{clb}, V_{des}	83.3 m s^{-1}
Cruise speed V_{cr}	152.8 m s^{-1}
Cruise range R	800 km
Field elevation of the airport h_a	0 m
Cruise altitude h_{cr}	7500 m
Air density (takeoff) ρ^{to}	1.225 kg m^{-3}
Air density (climb and descent) ρ^{clb}, ρ^{des}	0.9075 kg m^{-3}
Air density (cruise and reserve) ρ^{cr}	0.59 kg m^{-3}
Battery pack energy density e_b	440 W h kg^{-1}

TABLE IV
EFFICIENCY OF ELECTRIC PROPULSION SYSTEM COMPONENTS IN AEA [4], [37]

Component	**Value**
Electric motor + inverter efficiency $\eta_{em,inv}$	95%
PMAD* efficiency η_{PMAD}	96%
Battery efficiency η_{bat}	95%
Propulsive efficiency during cruise η_{prop}	87%
* PMAD: power management and distribution system	

Authorized licensed use limited to: TU Delft Library. Downloaded on August 13,2026 at 11:22:15 UTC from IEEE Xplore. Restrictions apply.

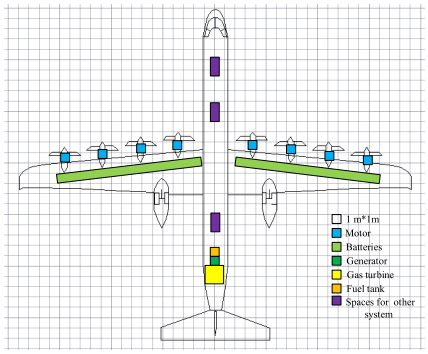


Fig. 10. Central generator architecture in aircraft layout.

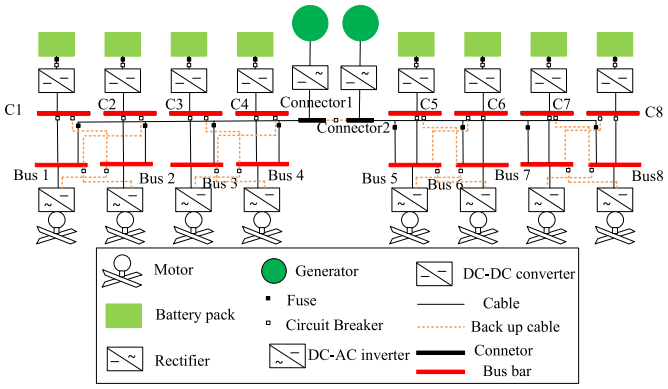


Fig. 11. Proposed electrical architecture for AEA with eight battery packs, cross-redundant bus structure, and DC–DC converters.

To account for capacity fade, we also evaluate an end-of-life (EOL) case with 80% remaining pack energy, i.e., $E_{\text{pack,EOL}} = 0.8 \times E_{\text{pack,BOL}} = 12\,518.4$ kWh. Assuming the same mission profile and that both cruise energy scale linearly with cruise time (and, thus, range), the achievable range at EOL is reduced from 800 to approximately 568 km (71% of the baseline). This provides a first-order degradation-aware estimate of operational range and highlights the sensitivity of mission capability to capacity retention.

III. Architecture Design and Evaluation of Electrical Power Systems in AEA

Depending on the location of the generator, the AEA design schematic can be categorized into two types: central architecture and symmetric architecture [3]. In the central architecture, the generators are located at the tail of the aircraft. In the symmetric architecture, the generators are positioned on each wing of the aircraft [3]. The central generator architecture is generally preferred for AEAs as it offers a better weight distribution, improved stability, reduced structural stress, and shorter electrical and fuel lines. In Fig. 10, the bus bars and battery packs are symmetrically distributed along the wings to ensure balanced power distribution and optimized weight characteristics. At the same time, the generators are located at the tail of the aircraft.

For electrical power system architecture, there are three different topologies commonly used in the design. These topologies vary in the number and structure of bus bar configurations, including ring structures, cross-redundant structures, and H-type structures [3], [11], [38]. The ring structure offers reliability through rerouting capabilities but results in the heaviest system [3], while the H-type bus bar structure has lower reliability than the cross-redundant structure [3]. This study utilizes a cross-redundant bus bar, which provides the highest reliability and the lowest weight due to its multifeeder and multisource configuration [3]. Multiple smaller batteries are employed in AEAs instead of a single large unit to enhance redundancy and safety, while generators serve as backup power sources during the reserve phase.

A. Electrical Power System Architecture Design in AEA

The entire power distribution system in an AEA has a different voltage level design compared to traditional aircraft. The MW- and kV-level voltage architecture is designed to serve various loads in an AEA. Therefore, DC–DC converters, DC–AC inverters, and rectifiers are used in the electrical architecture to provide suitable voltage levels for different subsystems. The DC–DC converter plays a crucial role in regulating and stepping down high-voltage DC to lower voltage levels required by onboard systems. Moreover, the DC–AC inverter converts DC power into AC to drive the electric motors. A rectifier converts AC power from generators into DC power to supply the DC buses. Fuses are employed to disconnect the circuit from the batteries as a protective measure in the event of a short circuit. Only a limited number of circuit breakers are used in the architecture, as more circuit breakers can increase the overall failure rate. Fig. 11 illustrates an electrical architecture containing all the components mentioned above. The solid lines represent the primary feed to the motors, while the dotted orange lines indicate secondary feeds from separate buses.

In an AEA, there are two functions for DC–DC converters. The first is to provide lower voltages for nonpropulsive loads, such as the environmental control system and thermal management system, which typically require 270-V DC. In that case, the DC–DC converters in the power distribution system regulate and step down the high voltage to 270- and 28-V levels. The second is to supply high voltage for the electric motors. Battery voltages can vary during flight depending on their state of charge. A key purpose of using DC–DC converters is to stabilize the bus voltage for the motors. The power density of MW-level converters is typically 10–15 kW/kg, meaning that a 1–2-MW converter would weigh over 100 kg. In the overall architecture, the total weight of the converters exceeds 1000 kg. Alternatively, the electric motors can be designed to tolerate a wider voltage range, eliminating the need for DC–DC converters. In this configuration, both the high-voltage 3-kV battery and 3-kV motor are designed with voltage tolerance to improve system performance. Under this configuration, the cabling system must then be capable of carrying higher current at the lowest battery voltage, which is discussed in the cable design section. In addition, the higher voltage stress makes machine insulation design more challenging, particularly under low-pressure aerospace conditions, where

Authorized licensed use limited to: TU Delft Library. Downloaded on August 13,2026 at 11:22:15 UTC from IEEE Xplore. Restrictions apply.

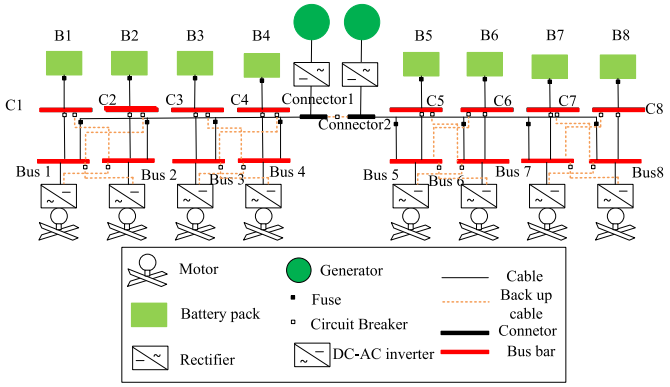


Fig. 12. Improved electrical architecture for AEA with eight battery packs and a cross-redundant bus, with DC–DC converters eliminated.

TABLE V
COMPONENT SPECIFIC FAILURE RATES OF REFERENCE APPLICATIONS AND RESULTING FAILURE PROBABILITY [41], [42]

Component	λ	Failure rate per million hours in the reference application	Component specific failure probabilities
Battery fault	λ_B	9.3 failures	30.5%
Circuit breaker fault	λ_{Cb}	5.3 failures	17.4%
Busbar fault	λ_{Bb}	0.25 failures	0.8%
Cable fault	λ_C	0.25 failures	0.8%
DC-AC inverter fault	λ_{in}	4.75 failures	15.6%
Rectifier fault	λ_{re}	4.75 failures	15.6%
Motor fault	λ_M	5.9 failures	19.3%

partial-discharge-related constraints become more severe [39], [40]. Consequently, the practical design of electric motors must carefully balance these system-level advantages against the requirements for insulation robustness and resilience to PD. In terms of efficiency, higher operating voltage can reduce the current required for a given power level and, therefore, lower winding copper losses. However, this benefit may be partly offset at the machine level by the more demanding insulation requirements, which can reduce slot fill factor and affect thermal dissipation. This configuration eliminates the need for DC–DC converters. The improved electrical architecture is presented in Fig. 12.

B. Evaluation of Electrical Power System Architecture in AEA

The evaluation criteria include reliability and weight. Among these, reliability is the most critical factor [12].

1) Reliability: The reliability of the system ensures the overall safety of the aircraft [15]. The design must satisfy strict safety requirements to minimize the risk of catastrophic failure. Failure modes can be categorized according to the components involved, including batteries, motors, circuit breakers, cables, and other components. Table V presents the failure rates and corresponding failure probabilities of different components, with values compiled from multiple [12], [41], [42].

TABLE VI
RISK IMPACT OF THE SINGLE COMPONENTS

Mode	Effect	Power loss	Risk impact
Battery failure	Reduced 1/8	12.5%	0.0380
Busbar failure	Reduced 1/8	12.5%	0.0001
Motor busbar failure	Reduced 1/8	12.5%	0.0001
Battery cable failure	Reduced 1/8	12.5%	0.0001
Motor cable failure	Reduced 1/8	12.5%	0.0001
DC-AC inverter failure	Reduced 1/8	12.5%	0.0195
Rectifier failure	Reduced 1/2	50%	0.0780
Motor failure	Reduced 1/8	12.5%	0.0241
Overall impact			**0.16**

Failure analysis is conducted through fault tree analysis and reliability block diagram to identify system-level effects of component failures. Failure modes and effects analysis (FMEA) is performed using three criteria: fault severity, fault occurrence, and fault impact [43]. The impact of a fault is calculated as the product of its occurrence probability and severity

$$\text{Risk impact} = F \times S \tag{23}$$

where F is the component-specific failure probability and S is the fault severity represented by the associated power loss. All failure rate values are normalized for an operating time of one million hours [12]. After performing the FMEA by combining the probability of component failure with the severity of the power loss, the summarized results for the risk impact of the single components are presented in Table VI.

Ensuring the reliability of the electric propulsion system requires evaluating the combined impact of multiple component failures. According to aviation safety standards, the probability of a catastrophic aircraft-level failure must remain below 10^{-9} per flight hour [19]. The combined impact of multiple component failures is evaluated using a combinatorial framework that accounts for the number of distinct failure combinations among identical components. This formulation relies on the assumptions of statistically independent failure events. While common cause failures exist in real systems, this assumption is consistent with established practice in preliminary aircraft system reliability analyses [17], [18] and enables systematic comparison across architectures at the conceptual design stage. Binomial coefficients are used to represent the number of possible simultaneous failure combinations and are widely adopted in preliminary aircraft system reliability analyses. Higher-order failure combinations involving three or more components are excluded from this study, as these have a negligible influence on the overall catastrophic failure probability. These associated probabilities are several orders of magnitude lower than those of the dominant two-component failure modes. In this architecture, propulsion is supplied through four power paths, including motors, the power

Authorized licensed use limited to: TU Delft Library. Downloaded on August 13,2026 at 11:22:15 UTC from IEEE Xplore. Restrictions apply.

distribution from cable to motor bus bar to motor, the power distribution from battery to battery bus bar, and batteries. Therefore, the loss of any one part may result in complete system power loss. The following subsection provide the structured reliability calculation for each major subsystem.

The first catastrophic contributor is the failure of the motor subsystem, including both the motors and the cables/bus bars that supply them. λ_M is the failure rate of a single motor, with a rate of 5.9 failures per million hours. With eight motors, propulsion becomes unsafe when two or more motors fail simultaneously [42]. Here, C_8^k is the binomial coefficient, representing the number of ways k motors can fail out of eight. Thus, the term $C_8^k(\lambda_M)^k$ corresponds to the contribution of exactly k simultaneous motor failures to the catastrophic failure rate. In addition to motor faults, catastrophic failure may occur if the motor side distribution network loses sufficient cables or bus bars. These scenarios include the loss of both feeder cables to two independent motors, as well as failures involving two motor bus bars combined with cable failures along the remaining paths from the battery bus bar to the motor bus bar. For example, the total number of combinations for selecting two cables out of 16 cables is $16!/(2! \times 14!)$, which is equal to C_{16}^2. The probability that two specific cables feeding the same motor fail among the 16 connections is, therefore, given by $(C_{16}^1 C_1^1)/C_{16}^2$. For the next motor, with 14 remaining connections, the corresponding probability is $(C_{14}^1 C_1^1)/C_{14}^2$.

a) Motor-side catastrophic failure rate:

$$\lambda_{\text{motor}} = C_8^2 (\lambda_M)^2 + \frac{C_{16}^1 2! \times 14!}{16!} \lambda_C^2 \frac{C_{14}^1 2! \times 12!}{14!} (\lambda_C + \lambda_{Cb})^2 + C_8^2 \left(\lambda_{Bb} + (\lambda_C + \lambda_{Cb})^2\right)^2. \quad (24)$$

Catastrophic failure may also occur on the battery side. Types of failures include all failures of all eight batteries, the failure of all battery cables, the failure of two generator cables, the combination failure of four battery cables and one generator cable, and the combination failure of four battery bus bars and one generator bus bar.

b) Battery-side catastrophic failure rate:

$$\lambda_{\text{battery}} = (\lambda_B)^8 + (\lambda_C)^8 + (\lambda_C)^2 + C_8^4 (\lambda_C)^4 C_2^1 \lambda_C + C_8^4 (\lambda_{Bb})^4 C_2^1 \lambda_{Bb}. \quad (25)$$

Using the component failure rates given in Table V, the catastrophic failure rates of individual subsystems are calculated as shown in Table VII. The overall catastrophic failure rate is dominated by the two-motor-failure term, while all other multicomponent failure combinations are several orders of magnitude smaller and, therefore, have a negligible contribution. The resulting catastrophic failure rate is 9.77×10^{-10} per flight hour, which satisfies the aviation reliability requirement of 1×10^{-9} failures per flight hour [19]. The APU supplies the aircraft auxiliary loads, and its energy consumption is included in the mission energy calculation. However, the APU is not considered as a backup power source for the propulsion system in the reliability analysis because its power level is significantly smaller than the propulsion power demand. Consequently, the reliability evaluation focuses on the primary propulsion power architecture, which represents a conservative assumption. It should also be noted that removing the DC–DC converters slightly reduces the total component count and, therefore, marginally lowers the overall failure rate, leading to a small improvement in system reliability. Without DC–DC converters, the propulsion motors must operate over a wider input voltage range, which may influence motor reliability and potentially affect the motor failure rate depending on the motor design.

TABLE VII
FAILURE RATE OF CATASTROPHIC FAILURE

Failure type	Failure rate
Two motor failures	9.75×10^{-10}
Cables to two motors failure	3.95×10^{-26}
Two motor busbars with cable failure	1.75×10^{-12}
Eight batteries failure	5.60×10^{-41}
Eight batteries' cables failure	1.53×10^{-53}
Two generators' cables failure	6.25×10^{-14}
Four batteries' cables and one generator's cable failure	1.37×10^{-31}
Four battery busbars and one generator busbar failure	1.37×10^{-31}
Overall impact	9.77×10^{-10}

This value represents a best-case estimate, as the failure rates used in this analysis are derived from reference applications under nominal operating conditions and assume statistically independent component failures. In practical aircraft power systems, common-cause failures may occur due to thermal coupling, vibration effects, aging effects, and electrical overstress under transient or extreme operating conditions. All these factors potentially lead to correlated failures among nearby cables, bus bars, and power electronics. Such correlated effects could increase the true system-level failure rate beyond the value reported here. The present reliability evaluation is, therefore, intended for preliminary architecture comparison under nominal operating conditions. Future work will extend the model by incorporating fault propagation and common-cause failure mechanisms to more accurately capture system behavior under transient and extreme operating conditions.

2) Weight: The target mass of the powertrain group should be no more than 42 500 kg [19]. The total mass of the power distribution system, including the generators, batteries, bus bars, cables, and motors, is calculated. For the batteries, the required energy is defined by the aircraft's flight mission performance requirements. Consequently, the total battery weight remains unchanged regardless of the number of packs. To calculate the cables and bus bars [12], the estimation is based on the estimated aircraft dimensions [12]. The lengths of all cables connecting different buses are calculated and summarized in Table VIII, forming the foundation for weight calculation and conductor sizing

$$\text{Cable weight} = \text{Cable length} \times m_{\text{total}}. \quad (26)$$

Cable selection affects the evaluation of electrical network topologies, particularly with respect to weight and reliability.

Authorized licensed use limited to: TU Delft Library. Downloaded on August 13,2026 at 11:22:15 UTC from IEEE Xplore. Restrictions apply.

TABLE VIII
CABLE LENGTH IN DESIGNED ARCHITECTURE

From	To	Length(m)	From	to	Length(m)
G1	connector 1	10	G2	Connector 2	10
Connector 1	Bus 1	22	C4	Bus 4	4
Connector 1	Bus 2	17	C4	Bus 5	15
Connector 1	Bus 3	12	C5	Bus 4	15
Connector 1	Bus 4	7	C5	Bus 5	4
Connector 2	Bus 8	22	C6	Bus 6	4
Connector 2	Bus 7	17	C6	Bus 5	7
Connector 2	Bus 6	12	C7	Bus 7	4
Connector 2	Bus 5	7	C7	Bus 6	7
C1	Bus 1	4	C8	Bus 8	4
C1	Bus 2	7	C8	Bus 7	7
C2	Bus 2	4	B1-B8	C1-C8	8
C2	Bus 3	7	Bus 1-8	M1-8	72
C3	Bus 3	4	C3	Bus 4	7

TABLE IX
TOTAL POWER DISTRIBUTION SYSTEM WEIGHT

Batteries	Cables and buses	Motors	Generators	Total weight
35 563.6 kg	403.8 kg	1090.9 kg	1090.9 kg	38 149.2 kg

In this study, cables with PFA and PTFE insulation and aluminum or copper conductors were considered. Aluminum conductors offer lower density, reducing total system weight and improving weight scores for topologies with longer cable runs. Conversely, copper conductors provide lower resistance and superior thermal performance, enhancing reliability. Insulation choice influences dielectric strength and thermal stability, further impacting overall reliability. These variations can shift the relative ranking of topologies depending on whether weight reduction or reliability is prioritized. The choice of conductor material, insulation type, and voltage level is discussed in the section on cable design. The key finding is that adopting 3-kV aluminum conductors with PFA insulation yields substantial weight savings compared to other configurations. This analysis primarily considers the weight of cables and bus bars, where the bus bars are selected as conventional metallic types rated at 500 A under 3 kV to satisfy current-carrying requirements. Each bus bar strip weighs approximately 5 kg, contributing to the total system mass [3], [44]. Following the established methodologies, the cable sizing and mass are estimated.

The total weight of the power distribution system comprises the masses of the generators, motors, batteries, cables, and bus bars. Based on the aircraft design, the propulsion system includes eight electric motors, each capable of delivering a continuous power output of 1.36 MW and a peak power output of 1.50 MW. Two generators are sized according to this power requirement. Assuming a specific power of 11 kW/kg for both generators and motors [4], their respective weights are calculated. It should be noted that the assumed motor operation over the full 3-kV battery voltage range represents a best-case design scenario. While wide-voltage operation may influence motor efficiency and insulation requirements, these effects are implicitly accounted for in the motor mass and performance assumptions summarized in Table IX. The removal of DC–DC converters, therefore, reflects a system-level tradeoff prioritizing weight reduction, with the understanding that practical motor designs must balance efficiency, thermal limits, and voltage tolerance. The results of these calculations are summarized in Table IX. The total estimated weight of the entire powertrain group is 38149.2 kg.

IV. CONCLUSION

In this article, a high-voltage electrical power system for an AEA was proposed. A design process for electrical components and architectures was developed using the Elysian E9X aircraft as a case study. The cable design method was presented, and the effects of insulation material, cable sizing, voltage level, and operating temperature were analyzed. The battery design process was also shown to meet the required energy and power demands. After designing the electrical components, the electrical distribution system architecture was evaluated based on reliability and weight. The main findings are summarized as follows.

1) The transmission analysis reveals that adopting a higher system voltage, such as 3 kV, with aluminum conductors and PFA insulation results in substantial weight savings. Choosing 150 °C as the normal operating temperature is an optimal design choice.
2) The AEA battery pack is sized based on aircraft performance specifications, considering different flight phases. Because it contributes more than 90% of the powertrain weight, battery energy density is the primary driver of performance metrics such as range and payload.
3) An evaluation process for cross-redundant power distribution system architectures in AEAs is presented, which meets reliability and weight targets.

Although the proposed framework is demonstrated using a 90-passenger AEA (Elysian E9X) as a case study, the underlying electrothermal cable sizing rules and the evaluation methodology are scalable and independent of aircraft size. By updating the input power levels, voltage ratings, cable lengths, and redundancy requirements, the same approach can be applied to smaller regional aircraft and larger transport-class platforms. Moreover, the proposed framework for reliability evaluation is architecture-driven and remains applicable to hybrid-electric configurations, such as battery–hydrogen fuel cell aircraft. In such systems, the dominant contributors to system reliability may shift from purely electrical components to mechanical, thermal management, or fuel cell subsystems. The process would reparameterize component failure rates and fault combinations according to the selected architecture. Nevertheless, the methodology presented enables a consistent and integrated assessment of weight and reliability across different propulsion concepts. As a result, the framework provides a generalizable design and evaluation approach for a wide range of future electric and hybrid-electric aviation platforms.

Authorized licensed use limited to: TU Delft Library. Downloaded on August 13,2026 at 11:22:15 UTC from IEEE Xplore. Restrictions apply.

Future work will focus on extending the proposed framework to incorporate transient electrothermal modeling to capture time-dependent temperature variations under propulsion-driven load profiles, particularly during takeoff and climb. The impact of forced convection cooling under realistic aircraft installation conditions will also be investigated to quantify potential reductions in conductor size and cable weight. In addition, future studies will consider installation-specific factors such as cable routing, airflow distribution, and thermal coupling with surrounding components. The exploration of advanced cable designs, including multilayer insulation structures, will also be pursued to improve dielectric performance and enable more efficient insulation thickness optimization under varying voltage and environmental conditions. From a reliability perspective, more detailed models incorporating common-cause failures and mission-based analysis will be developed. Finally, experimental validation of the proposed electrothermal–dielectric framework will be conducted to support its application in practical aircraft design.

REFERENCES

[1] K. Ni et al., "Electrical and electronic technologies in more-electric aircraft: A review," *IEEE Access*, vol. 7, pp. 76145–76166, 2019.

[2] J.-A. Wolf, R. Meissner, A. A. Pohya, and G. Wende, "Flying electric: A comparative analysis of spare part demands and material cost for all-electric, hybrid-electric, and conventional aircraft propulsion systems," *Appl. Energy*, vol. 403, Jan. 2026, Art. no. 127036.

[3] R. Guo, J. Dong, R. E. Wolleswinkel, R. de Vries, and M. G. Niasar, "Electrical architecture of 90-seater electric aircraft: A cable perspective," *IEEE Trans. Transport. Electrific.*, vol. 11, no. 2, pp. 6854–6865, Apr. 2025.

[4] R. de Vries, R. E. Wolleswinkel, M. Hoogreef, and R. Vos, "A new perspective on battery-electric aviation, part II: Conceptual design of a 90-seater," in *Proc. AIAA SCITECH Forum*, Jan. 2024, p. 1490.

[5] J. Jiang et al., "A review on insulation challenges towards electrification of aircraft," *High Voltage*, vol. 8, no. 2, pp. 209–230, Apr. 2023.

[6] A. Saha, A. Azizi, and M. Ghassemi, "Optimal bipolar MVDC power cable designs for future wide-body all electric aircraft," *IEEE Trans. Dielectr. Electr. Insul.*, vol. 31, no. 4, pp. 2074–2083, Aug. 2024.

[7] A. Azizi and M. Ghassemi, "Design of high power density MVDC cables for wide-body all electric aircraft," *IEEE Trans. Dielectr. Electr. Insul.*, vol. 30, no. 5, pp. 2315–2324, Oct. 2023.

[8] C. E. D. Riboldi and F. Gualdoni, "An integrated approach to the preliminary weight sizing of small electric aircraft," *Aerosp. Sci. Technol.*, vol. 58, pp. 134–149, Nov. 2016.

[9] A. Bills, S. Sripad, W. L. Fredericks, M. Singh, and V. Viswanathan, "Performance metrics required of next-generation batteries to electrify commercial aircraft," *ACS Energy Lett.*, vol. 5, no. 2, pp. 663–668, Feb. 2020.

[10] A. Barzkar and M. Ghassemi, "Electric power systems in more and all electric aircraft: A review," *IEEE Access*, vol. 8, pp. 169314–169332, 2020.

[11] A. Siddavatam, K. Rajashekara, R. Reddy, H. Huang, H. Krishnamoorthy, and F. Wang, "A h ype architecture for electric/hybrid lectric aircraft propulsion systems," *IET Elect. Syst. Transp.*, vol. 13, no. 1, p. e12065, 2023.

[12] M. Hoffmann et al., "Early design stage evaluation of all electric aircraft power systems focusing on long-term behavior," *Energies*, vol. 17, no. 18, p. 4653, Sep. 2024.

[13] J. Li et al., "Weight-constrained reliability allocation for all-electric aircraft powertrains," *IEEE Trans. Transport. Electrific.*, vol. 10, no. 3, pp. 6596–6607, Sep. 2024.

[14] L. Setlak, R. Kowalik, A. Gebura, and P. Gołda, "Dynamic stability analysis of the aircraft electrical power system in the more electric aircraft concept," *Sci. Rep.*, vol. 14, no. 1, Oct. 2024, Art. no. 25521.

[15] V. Marciello, F. Orefice, F. Nicolosi, D. Ciliberti, and P. Vecchia, "Design of hybrid-electric aircraft with fault-tolerance considerations," *Chin. J. Aeronaut.*, vol. 36, no. 2, pp. 160–178, Feb. 2023.

[16] S. Liu, F. Guo, X. Wu, C. Wen, Y. Yang, and J. Chen, "A distributed secure and robust power management framework for more electric aircraft," *IEEE Trans. Transport. Electrific.*, vol. 10, no. 4, pp. 9248–9263, Dec. 2024.

[17] B. M. O'Halloran, R. B. Stone, and I. Y. Tumer, "Early design stage reliability analysis using function-flow failure rates," in *Proc. 23rd Int. Conf. Design Theory Methodol., 16th Design Manuf. Life Cycle Conf.*, Jan. 2011, pp. 455–464.

[18] Y. Li, "Reliability analysis of distributed electric aircraft propulsion system," in *Proc. 3rd Int. Conf. Energy, Power Electr. Technol. (ICEPET)*, May 2024, pp. 1388–1391.

[19] (2025). *IEEE/AIAA ITEC+EATS Student Design Competition*. [Online]. Available: https://itec-conf.com/app/uploads/2025/01/ITECStudent-Competition-1.pdf

[20] C. Wijnveen and R. van de Luijtgaarden, "Design of propulsion system for 9 pax electric aircraft," M.S. thesis, Dept. Elect. Sustain. Energy, Delft University of Technology, Delft, The Netherlands, 2022.

[21] T. L. Bergman, *Fundamentals of Heat and Mass Transfer*. Hoboken, NJ, USA: Wiley, 2011.

[22] G. Hewitt, G. Shires, and T. Bott, *Process Heat Transfer*. Boca Raton, FL, USA: CRC Press, 1994.

[23] E. Aretskin-Hariton, M. Bell, S. Schnulo, and J. S. Gray, "Power cable mass estimation for electric aircraft propulsion," in *Proc. AIAA AVIATION FORUM*, Aug. 2021, p. 3021.

[24] F. P. Incropera, D. DeWitt, T. Bergman, and A. Lavine, *Fundamentals of Heat and Mass Transfer*, 6th ed., Hoboken, NJ, USA: Wiley, 2007.

[25] Y. A. Cengel and M. A. Boles, "Thermodynamics: An engineering approach," *Sea*, vol. 1000, no. 8862, pp. 93–287, 2002.

[26] M. Bhide, Y. Liang, G. R. C. Mouli, M. Ghaffarian Niasar, and P. Bauer, "Hybrid reconfigurable battery pack for all-electric aircraft: Synergizing high-specific-energy and power battery types," in *Proc. IEEE Transp. Electrific. Conf. Expo (ITEC)*, Jun. 2024, pp. 1–6.

[27] (Oct. 2018). *Standard Practice for Design, Alteration, and Certification of Aircraft Electrical Wiring Systems*. [Online]. Available: https://store.astm.org/f2639-18.html

[28] Prysmian Group. (Oct. 2017). *Wires & Cables for Aerospace Applications*. [Online]. Available: https://www.prysmian.com/sites/default/files/atoms/files/Catalogue%20AEROSPACE.pdf

[29] (May 2017). *PTFE and PFA: Similarities and Differences*. [Online]. Available: https://www.emerson.com/documents/automation/white-paper-ptfe-pfa-similarities-differences-rosemount-en-585104.pdf

[30] H. Teng, "Overview of the development of the fluoropolymer industry," *Appl. Sci.*, vol. 2, no. 2, pp. 496–512, May 2012.

[31] F. C. Cheng, "Insulation thickness determination of polymeric power cables," *IEEE Trans. Dielectr. Electr. Insul.*, vol. 1, no. 4, pp. 624–629, Apr. 1994.

[32] Technology Corporation, Woburn, MA, USA. (2025). *Air Pressure at Altitude Calculator*. [Online]. Available: https://www.mide.com/air-pressure-at-altitude-calculator

[33] Y. Liang, D. Bodnár, G. Ram Chandra Mouli, D. Ragni, and P. Bauer, "Charging demand prediction: Small all-electric aircraft and electric vertical takeoff and landing aircraft," *IEEE Trans. Transport. Electrific.*, vol. 11, no. 1, pp. 2732–2747, Feb. 2025.

[34] C. E. D. Riboldi, "Energy-optimal off-design power management for hybrid-electric aircraft," *Aerosp. Sci. Technol.*, vol. 95, Dec. 2019, Art. no. 105507.

[35] J. D. Anderson and M. L. Bowden, *Introduction to Flight*, vol. 582, 8th ed., New York, NY, USA: McGraw-Hill, 2016.

[36] A. R. Gnadt, R. L. Speth, J. S. Sabnis, and S. R. H. Barrett, "Technical and environmental assessment of all-electric 180-passenger commercial aircraft," *Prog. Aerosp. Sci.*, vol. 105, pp. 1–30, Feb. 2019. [Online]. Available: https://www.sciencedirect.com/science/article/pii/S0376042118301179

[37] R. E. Wolleswinkel, R. de Vries, M. Hoogreef, and R. Vos, "A new perspective on battery-electric aviation, part I: Reassessment of achievable range," in *Proc. AIAA SCITECH Forum*, Jan. 2024, p. 1489.

[38] M. Ghassemi, A. Barzkar, and M. Saghafi, "All-electric NASA N3-X aircraft electric power systems," *IEEE Trans. Transport. Electrific.*, vol. 8, no. 4, pp. 4091–4104, Dec. 2022.

[39] V. Madonna, P. Giangrande, W. Zhao, H. Zhang, C. Gerada, and M. Galea, "Electrical machines for the more electric aircraft: Partial discharges investigation," *IEEE Trans. Ind. Appl.*, vol. 57, no. 2, pp. 1389–1398, Mar. 2021.

[40] A. Saha and M. Ghassemi, "A review of electrical insulation challenges for electrical powertrain components in the future more- and all-electric aircraft under low-pressure conditions," *IEEE J. Emerg. Sel. Topics Power Electron.*, vol. 13, no. 4, pp. 4521–4536, Aug. 2025.

Authorized licensed use limited to: TU Delft Library. Downloaded on August 13,2026 at 11:22:15 UTC from IEEE Xplore. Restrictions apply.

[41] M. V. Bendarkar, D. Sarojini, E. Harrison, and D. N. Mavris, "Evaluation of off-nominal performance and reliability of a distributed electric propulsion aircraft during early design," in *Proc. AIAA Scitech Forum*, Jan. 2021, p. 1723.
[42] T. Ter Horst, F. Walterbos, *Design & Reliability Assessment of Aea Propulsion Grid*. [Online]. Available: https://repository.tudelft.nl
[43] Y. Wang, X. Gao, Y. Cai, M. Yang, S. Li, and Y. Li, "Reliability evaluation for aviation electric power system in consideration of uncertainty," *Energies*, vol. 13, no. 5, p. 1175, Mar. 2020.
[44] T. Dakin, "Breakdown of gases in uniform fields-paschen curves for nitrogen, air and sulfur hexafluoride," *Electra*, vol. 32, pp. 61–82, Aug. 1974.



Tiantian Xu (Member, IEEE) received the B.Sc. degree in building facilities intelligence technology from Chang'an University, Xi'an, China, in 2014, and the M.Sc. degree in electrical power from Newcastle University, Newcastle Upon Tyne, U.K., in 2019. She is currently pursuing the Ph.D. degree with Delft University of Technology, Delft, The Netherlands.

Her research interests include partial discharge monitoring, diagnostics, and residual lifetime estimation for aircraft cables for electric aircraft, energy conversion, and storage group.



Jawad Ahmad (Member, IEEE) is currently pursuing the Ph.D. degree with the High Voltage Technologies Group, Department of Electrical Sustainable Energy, Delft University of Technology, Delft, The Netherlands.

He is currently conducting research on the study of aging mechanisms in aircraft cables, with a focus on the performance evaluation of cables under different stress conditions. His research interests also include novel dielectric materials for next-generation insulation systems.



Yawen Liang (Member, IEEE) received the B.Sc. degree in electrical engineering from Sichuan University, Chengdu, China, in 2020, and the M.Sc. degree (cum laude) in electrical engineering, from Delft University of Technology, Delft, The Netherlands, in 2022, where she is currently pursuing the Ph.D. degree in battery systems and power electronics interfaces for electric aircraft with the DC systems, energy conversion, and storage group.



Gautham Ram Chandra Mouli (Senior Member, IEEE) received the bachelor's degree in electrical engineering from the National Institute of Technology, Trichy, India, in 2011, the master's degree in electrical engineering from the Delft University of Technology, Delft, The Netherlands, in 2013, and the Ph.D. degree from the Delft University, Delft, in 2018, with a focus on the development of a solar-powered V2G electric vehicle charger.

He is an Associate Professor at the DC systems, Energy conversion and Storage Group, Department of Electrical Sustainable Energy, Delft University of Technology. From 2017 to 2019, he was a Post-Doctoral Researcher at TU Delft, Delft. His research is on EV batteries, power converters for EV charging, smart charging of EVs, and trolley buses. He is the Coordinator and a Lecturer for the Massive Open Online Course (MOOC) on Electric cars on edX.org with 235 000 learners from 175 countries. He is involved in many projects at the national and EU levels on electric mobility and batteries, including Flexinet, TULIPS, FLOW, Drive2X, and NEON. His current research focuses on EV batteries, EV charging and vehicle-to-grid (V2G), and grid integration of EVs.

Dr. Chandra Mouli received the "Most Significant Innovation in Electric Vehicles" Award from IDtechEx in 2018 and the "Best Tech Idea of 2018" by KIJK. He was awarded the Best Paper Prize for IEEE TRANSACTIONS ON INDUSTRIAL INFORMATICS in 2018, the Best Poster Prize at Erasmus Energy Forum 2016, The Netherlands, and the Best Paper Prize at the IEEE INDICON Conference 2009, India. He is the Vice-Chair of IEEE Industrial Electronic Society Benelux chapter.



Mohamad Ghaffarian Niasar (Member, IEEE) was born in Tehran, Iran, in 1984. He received the M.Sc. degree in electrical power engineering from the Sharif University of Technology, Tehran, in 2008, and the Ph.D. degree in electrical engineering from the Royal Institute of Technology, Stockholm, Sweden, in 2015.

He is currently an Associate Professor with the High Voltage Technologies Group, Delft University of Technology, Delft, The Netherlands. His research interests include electrical insulation aging, insulation systems for power electronics-based devices, partial discharges, medium-frequency power transformers, power cables, and FEM modeling.

Authorized licensed use limited to: TU Delft Library. Downloaded on August 13,2026 at 11:22:15 UTC from IEEE Xplore. Restrictions apply.